Utilizing Carbon Nanotube Electrodes to Improve Charge Injection and Transport in Bis(trifluoromethyl)-dimethyl-rubrene Ambipolar Single Crystal Transistors

Wei Xie,[†,*] Pradyumna L. Prabhumirashi,[‡] Yasuo Nakayama,[§] Kathryn A. McGarry,[⊥] Michael L. Geier,[‡] Yuki Uragami,[§] Kazuhiko Mase,[∥] Christopher J. Douglas,[⊥] Hisao Ishii,[§] Mark C. Hersam,[‡] and C. Daniel Frisbie[†,*]

[†]Department of Chemical Engineering and Materials Science, University of Minnesota, 421 Washington Avenue SE, Minneapolis, Minnesota, 55455, United States, [‡]Department of Materials Science and Engineering and Department of Chemistry, Northwestern University, 2220 Campus Drive, Evanston, Illinois 60208, United States, [§]Graduate School of Advanced Integration Science, Chiba University, 1-33 Yayoi-cho, Inage-ku, Chiba 263-8522, Japan, [⊥]Department of Chemistry, University of Minnesota, 207 Pleasant Street SE, Minneapolis, Minnesota, 55455, United States, and [∥]Institute of Materials Structure Science, High Energy Accelerator Research Organization (KEK), 1-1 Oho, Tsukuba, Ibaraki 305-0801, Japan

ABSTRACT We have examined the significant enhancement of ambipolar charge injection and transport properties of bottom-contact single crystal field-effect transistors (SC-FETs) based on a new rubrene derivative, bis(trifluoromethyl)-dimethyl-rubrene (fm-rubrene), by employing carbon nanotube (CNT) electrodes. The fundamental challenge associated with fm-rubrene crystals is their deep-lying HOMO and LUMO energy levels, resulting in inefficient hole injection and suboptimal electron injection from conventional Au electrodes due to large Schottky barriers. Applying thin layers of CNT network at the charge injection interface of fm-rubrene crystals substantially reduces the contact resistance for both holes and electrons; consequently, benchmark ambipolar mobilities have been achieved, reaching 4.8 $cm^2 V^{-1} s^{-1}$ for hole transport and 4.2 $cm^2 V^{-1} s^{-1}$ for electron transport. We find that such improved injection efficiency in fm-rubrene is beneficial for ultimately unveiling its intrinsic charge transport properties so as to exceed those of its parent molecule, rubrene, in the current device architecture. Our studies suggest that CNT electrodes may provide a universal approach to ameliorate the charge injection obstacles in organic electronic devices regardless of charge carrier type, likely due to the electric field enhancement along the nanotube located at the crystal/electrode interface.

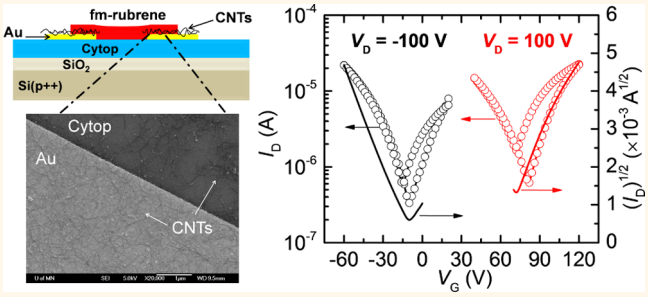

KEYWORDS: ambipolar transport · rubrene derivative · CNT · charge injection · Schottky barrier

Charge carrier injection from metal contacts into organic semiconductors is a critical process controlling the performance of optoelectronic devices such as organic light-emitting diodes (OLEDs) and organic field-effect transistors (OFETs).[1] The complexity at the metal/organic semiconductor interface, for example, the presence of interfacial traps, local structural disorder of the semiconductor, and any additional effects induced by charge transfer, makes it a fundamentally challenging problem to systematically control and modify the charge injection process.[2] Large energetic barriers for hole or electron injection can be present when an offset exists between the metal work function and the highest occupied molecular orbital (HOMO) or the lowest unoccupied molecular orbital (LUMO) of the organic semiconductor. Under these circumstances, charge injection becomes the limiting factor for the subsequent device operation, often manifested by large contact resistance and nonohmic current–voltage behavior, consequently resulting in an underestimate of the intrinsic electrical properties of the semiconductor. Efficient charge injection is, therefore, particularly important in OFETs

* Address correspondence to xiexx097@umn.edu, frisbie@umn.edu.

Received for review September 1, 2013 and accepted October 24, 2013.

Published online October 25, 2013
10.1021/nn4045694

based on organic single crystals, which is the ideal system to probe the intrinsic charge transport and structure–property correlation of the semiconductor material.[3]

Several techniques have been developed to address the charge injection problem for one type of carrier, either holes or electrons, in organic electronic devices.[4–11] One general strategy employs surface modifiers to change the metal work function through interface-dipole induced vacuum-level shifts in order to align the Fermi energies with the energy levels of the semiconductor. For example, different thiol-type self-assembled monolayers (SAMs) have been used to modulate the work function of Au and Ag.[4] Recently, the aliphatic amine-functionalized polymers have been found to greatly reduce the work functions for a wide variety of conductors including high work function metals (*e.g.*, Au, Ag), transparent conductive metal oxides and conducting polymers, thereby providing an excellent alternative to low work function metals (*e.g.*, Ca, Al) for n-type organic semiconductor devices.[6] Another option utilizes chemical doping of the semiconductor to increase its local conductivity and/or to fill up the interfacial traps, and thus decrease the injection barrier height. For p-type organic semiconductors, strong electron acceptors such as F_4-TCNQ and $FeCl_3$ have often been used as dopants.[7–9] However, the exact nature of the doping mechanism along with the knowledge about the dopant concentration and its location remains unclear. Alternative approaches have involved depositing other conducting or semiconducting films, often ultrathin metal oxides, as the charge transport layer or tunneling layer between the metal contact and semiconductor.[10,11] Nevertheless, the deposition of oxide films is often performed under less favorable conditions, usually accompanied by high-temperature processes and tedious patterning steps.

The techniques described above have been successfully applied to organic thin film devices but are less used in single crystals. In fact, most carefully studied high-mobility p-type (*e.g.*, rubrene, TMTSF, DNTT)[12–15] or n-type organic crystals (*e.g.*, PDIF-CN_2)[16] do not seem to experience charge injection difficulties with commonly used Au electrodes. One apparent reason is that their respective HOMO or LUMO levels align close to the Au work function (5.0 eV). Somewhat surprisingly, the benchmark material, rubrene single crystal, having a HOMO level of 4.9 eV, can form high-quality ohmic contacts with several electrode materials such as evaporated Au films[17]and Ag films,[18] and aqueous graphite paint,[19] leading to large room-temperature hole mobilities of 10 $cm^2\ V^{-1}\ s^{-1}$. This fortunate advantage has directly facilitated a variety of important fundamental transport studies using rubrene crystals, such as the observation of band-like transport,[20,21] unusual conductivity behavior at high charge densities,[22–24] surface doping using molecular SAMs,[19] and determination of long exciton diffusion lengths and related photooxidation phenomena.[25,26]

During our efforts to investigate the structure–property relationships in rubrene crystals, we have previously developed a series of new rubrene derivatives and have fabricated single crystal OFETs (SC-OFETs) from these rubrenes.[27] Remarkably, the SC-OFETs built on bis(trifluoromethyl)-dimethyl-rubrene (molecular structure shown in Figure 1(a)), which we will refer to as fm-rubrene, exhibit ambipolar transport behavior with high hole mobility of 1.5 $cm^2\ V^{-1}\ s^{-1}$ and electron mobility of 0.28 $cm^2\ V^{-1}\ s^{-1}$. Despite this preliminary achievement, the fm-rubrene SC-OFETs have yet to reach their expected intrinsic electrical performance, on the basis of band structure calculations that suggest superior transport properties (for both holes and electrons) over the parent molecule, rubrene.[27] We speculated that this was because the side group functionalization in fm-rubrene led to deeper HOMO and LUMO levels than rubrene, which had an adverse impact on the hole injection when using the same Au electrodes. Electron injection was easier than in rubrene, as seen in our previous report, but was still not optimized.[27] As a result, SC-OFETs built on fm-rubrene using Au electrodes suffer from suboptimal charge injection. Engineering the contacts is therefore critical for this novel ambipolar crystal to realize its true transport potential as predicted by theory.

In this article, we demonstrate a universal approach, rather than simply modulating the work function of the electrode material, to enhance the ambipolar injection characteristics for fm-rubrene crystals. In particular, we utilize single-walled carbon nanotube (CNT) electrodes to simultaneously enhance the injection properties for both charge carriers in Cytop-gated, bottom-contact ambipolar fm-rubrene SC-OFETs. We show that the presence of randomly oriented CNT networks at the charge injection interface, either serving as a standalone electrode or forming a hybrid electrode with Au, results in substantial improvement in contact resistance for *both* hole and electron injection. Concurrently, the resulting fm-rubrene SC-OFETs show maximum hole mobility μ_h of 4.8 $cm^2\ V^{-1}\ s^{-1}$ and electron mobility μ_e of 4.2 $cm^2\ V^{-1}\ s^{-1}$, respectively, setting a record for wide bandgap, ambipolar, conjugated organic semiconductors. We systematically investigate the dependence of contact conditions, in terms of the CNT density, on fm-rubrene device performance. The optimized fm-rubrene SC-OFETs show hole transport properties comparable to, and electron transport properties greatly exceeding those of rubrene SC-OFETs in the current device structure. The fm-rubrene devices with engineered contacts also exhibit enhanced low-temperature ambipolar transport behavior. Our present work on a new organic single crystal system, combined with other research efforts employing CNT electrodes in different device architectures,[28–35] advocates the utility of CNTs as efficient contacts to alleviate the injection difficulties

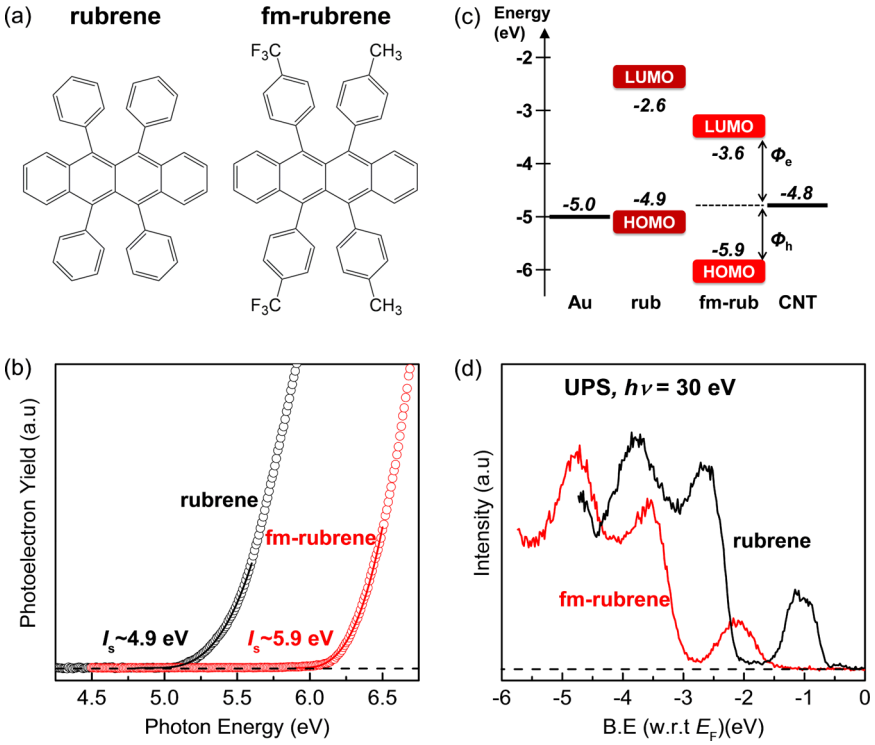

Figure 1. (a) Molecular structures of rubrene and fm-rubrene. (b) Photoelectron yield spectroscopy (PYS) spectra of rubrene (black, open circles) and fm-rubrene crystals (red, open circles). The solid lines are least-squares cubic-fitting results. I_s is the ionization energy. (c) Energy level diagram of Au, CNT, and HOMO/LUMO levels of rubrene and fm-rubrene. Φ_e and Φ_h are the barrier heights for electron and hole injections, respectively. (d) Ultraviolet photoelectron spectroscopy (UPS) spectra (normalized by incident photon flux) of rubrene (black lines) and fm-rubrene crystals (red lines) around the HOMO peak. Binding energy (B.E.) with respect to the Fermi level (E_F) is taken as the *x*-axis. Incident photon energy is 30 eV.

regardless of charge carrier polarity in organic optoelectronic devices.

RESULTS AND DISCUSSION

The single crystals (fm-rubrene, rubrene) utilized in this work were grown by physical vapor transport.[36] The vapor-grown fm-rubrene crystals belong to the *Cmca* space group (the same space group as rubrene), with lattice parameters of $a = 34.197$ Å, $b = 7.1577$ Å, $c = 14.052$ Å, $\alpha = \beta = \gamma = 90°$ (Table S1, Figures S1−S3 in Supporting Information (SI)). These crystals are in fact polymorphic to the solution-grown crystals reported previously, which belong to *Pbcm* space group,[27] and the unit cell dimensions and interlayer distances for the two polymorphs are the same (Table S2 in SI). The space group conservation and the preserved distances, in particular the π-stacking distance, validate the comparison of fm-rubrene to its parent molecule, rubrene, in the following single-crystal device studies.

The solid-state electronic structure of fm-rubrene single crystals was examined using ultraviolet photoelectron spectroscopy (UPS). Details of the photoelectron experimental setup can be found elsewhere.[37,38] Before the UPS measurement, the ionization energy (I_s) of a fm-rubrene crystal was determined using photoelectron yield spectroscopy (PYS), which probes the total photoemission current as a function of the incident photon energy, $h\nu$.[38,39] As shown in Figure 1(b), I_s of fm-rubrene and rubrene (used for comparison) can be extracted around the onset of photoelectron yield (Y) by least-squares fitting with the following relation, $Y \propto (h\nu - I_s)^3$. The evaluated I_s of rubrene and fm-rubrene are 4.90 and 5.94 eV, respectively. The result for the rubrene crystal is consistent with previously reported values.[38] On the other hand, the fm-rubrene crystal exhibits a strikingly deeper-lying HOMO level of 5.9 eV, as compared with other organic crystals that show p-type behavior.[40] By simply functionalizing the rubrene molecule with short trifluoromethyl/methyl groups, an astonishing deepening of the energy levels as large as 1 eV was obtained (bandgap ~2.3 eV determined from redox potentials remains unchanged[27]), highlighting the pronounced impact that the molecular structure has on the electronic structure. As a result, a large hole injection barrier is expected between fm-rubrene and Au (Figure 1(c)), presumably resulting in large contact resistance and underestimation of hole mobility, thereby supporting our previous conjecture of contact-limited charge transport in fm-rubrene SC-OFETs with Au electrodes.[27] The closer LUMO position to the Au work function is also in line with good electron transport in fm-rubrene transistors; however, an electron injection barrier as large as 1.4 eV still exists (deduced from Mott−Schottky rule of vacuum-level alignment in Figure 1(c)).

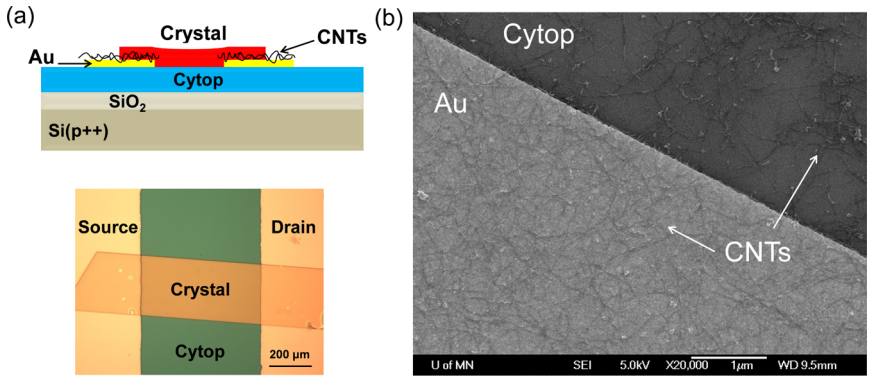

Figure 2. (a) Cross-sectional device structure (top) and optical micrograph (bottom) of a bottom-contact, Cytop-gated fm-rubrene SC-OFET. (b) Scanning electron micrograph (SEM) showing the CNT morphology on Au contacts and at the Au/Cytop interface in the high-density CNT/Au electrode.

We note that in the solution phase, when the intermolecular interaction is negligible, the measured oxidation potential of fm-rubrene is only ~0.1 eV larger than rubrene.[27] Calculations also predict a slightly larger adiabatic ionization potential (~0.2 eV) in the gas phase of fm-rubrene over rubrene.[27] These results indicate that the contribution of the aryl substituents to the energy level shift is relatively minor for individual rubrene molecules. As noted above, however, in the solid state, a significantly (~1 eV) deeper energy level was observed for fm-rubrene, as compared to rubrene, while rubrene exhibited similar HOMO levels measured in both solution phase and solid-state (~4.9 eV). We propose that the extra contribution to the energy level deepening arises from the large surface dipoles (due to the trifluoromethyl groups) leading to an increase in the work function. As seen in Figure S4 (Section 2 in SI), the surfaces of rubrene and fm-rubrene crystals both correspond to the π-stacking planes (for both rubrene and fm-rubrene, the $b-c$ plane). The long axes of the unit cells (a-axis) are perpendicular to the crystal surfaces. As a result, the $-CF_3$ and $-CH_3$ substituted phenyl side groups in the first molecular layer of fm-rubrene extend out from the surface, and a nonzero dipole moment is present at the surface. This can lead to a work function increase, *i.e.*, the surface dipoles provide an extra deepening of the HOMO level compared with a nonpolar surface in the case of rubrene, analogous to the increase in the work function of Au when coated with fluoroalkyl type SAMs.[4] Testing this hypothesis will help us to gain further insights into more rational molecular design for high-performance organic semiconductors with desired crystal packing and efficient charge injection.

Figure 1(d) shows the UPS spectra of rubrene and fm-rubrene crystals in the HOMO region plotted with respect to the Fermi level (E_F). The HOMO density of states (DOS) of fm-rubrene is nearly identical to the HOMO DOS of rubrene (*i.e.*, not affected by the functionalization of the side groups), yet it is apparent that the HOMO edge of fm-rubrene is further away from the E_F than that of rubrene. The HOMO peak width of 0.4 eV in fm-rubrene (as estimated by a single Gaussian fit) is also in good agreement with prior calculations.[27] A direct observation of valence band dispersion in the fm-rubrene crystal by angle-resolved photoelectron spectroscopy (ARPES) was prevented by spectrum broadening and insufficient spectral quality, likely due to sample charging. As a consequence, a quantitative analysis of the bandwidth and effective mass in fm-rubrene was difficult to carry out. Nevertheless, these photoelectron measurements have provided a baseline understanding of the solid-state electronic structure of fm-rubrene crystals, suggesting the importance of a suitable device fabrication strategy for realizing its intrinsic electrical properties.

SC-OFETs of fm-rubrene were constructed in a bottom-gate, bottom-contact architecture using Cytop as the insulator layer (Figure 2(a)). Cytop has been widely used as a high-quality dielectric material for OFETs due to its good bias-stress stability and low interfacial trap density.[41] The bottom-contact geometry was selected to prevent any undesired surface damage in the crystals during the fabrication of top contacts. Besides, we have previously shown that fm-rubrene transistors have better performance in top-contact geometry as compared to the bottom-contact geometry, thus making bottom contact a challenging structure to work with.[27] We started with untreated, bare Au electrodes as the source and drain contacts (denoted as Au electrode) upon which thin fm-rubrene crystals were laminated across. Simultaneously, as a control group, thin films of CNTs were deposited onto the Au electrodes before the crystal lamination. The CNTs were dispersed in an aqueous solution of 1−2 wt % sodium cholate (SC). The deposition process was carried out *via* aerosol jet printing (AJP) in ambient conditions. AJP has been applied to a wide variety of conductor, semiconductor, and dielectric solutions and is a powerful technique to print high-resolution, large-area flexible electronic devices and circuits.[42−45] As a well-established procedure for fabricating high-performance CNT electronic devices,[46−49]

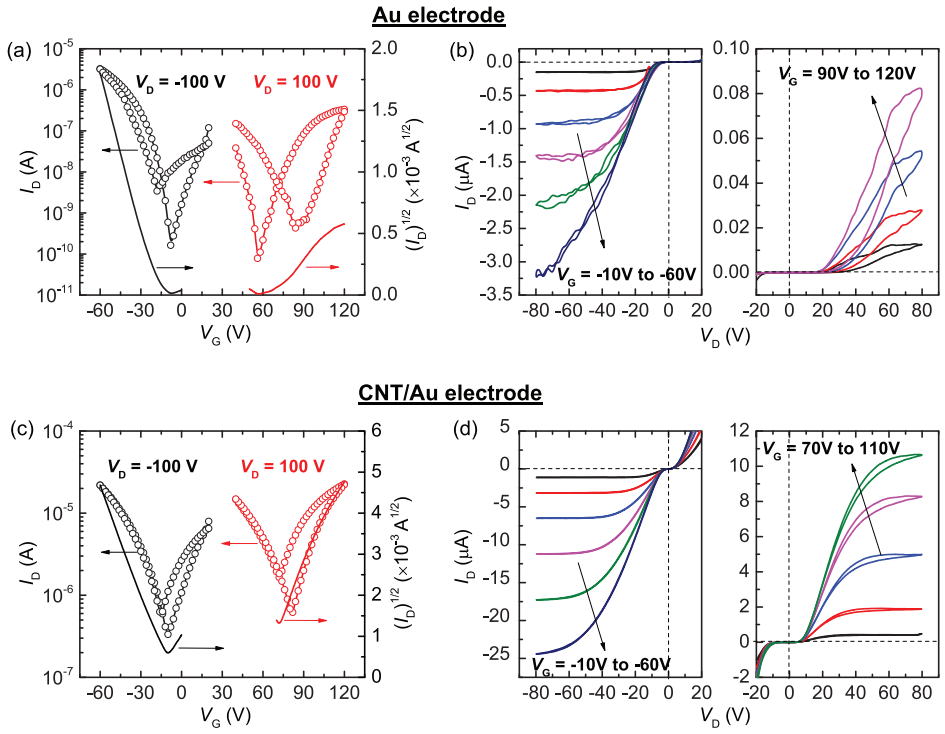

Figure 3. Device characteristics of Cytop-gated fm-rubrene transistors with Au electrodes (panels (a) and (b)), and high-density CNT/Au electrodes (panels (c) and (d)). (a), (c) Transfer curves (left axis, open circles) I_D-V_G in log−linear scale at $V_D = -100$ V (black) and $V_D = 100$ V (red); (right axis, solid lines) $(I_D)^{1/2}-V_G$ in linear scale at $V_D = -100$ V (black) and $V_D = 100$ V (red) for forward sweep only. (b), (d) Output curves I_D-V_D at several negative and positive V_G (in 10 V step). Device dimensions: (Au) $W = 250$ μm and $L = 520$ μm; (high-density CNT/Au) $W = 220$ μm and $L = 510$ μm.

the surfactants in the as-printed CNT films were removed by gentle rinsing with deionized (DI) water (see the details in Methods). As shown in the SEM image in Figure 2(b), the printed CNTs form a thin network of randomly oriented tubes (average length of a few μm) on top of the Au contacts and also extend slightly (<5 μm) into the channel. A direct bridging of CNTs between two electrodes was prevented because of the long channel length of typically 500 μm. The CNT coverage onto the Au electrode was controlled by varying the concentration of the CNT solution (see Figure S5 in SI) and was categorized into low (2−4 CNTs/μm), medium (5−15 CNTs/μm), and high (>20 CNTs/μm) density CNT/Au electrodes (see Figure S6 in SI). Additionally, a dense network of CNTs was printed as a stand-alone source/drain contact (denoted as CNT electrode; see Figure S6 in SI and Methods for further details).

Figure 3(a) shows the log−linear transfer characteristics of an fm-rubrene SC-OFET with Au electrodes showing ambipolar behavior. The saturation mobilities were $\mu_h = 1.34$ cm^2 V^{-1} s^{-1} and $\mu_e = 0.062$ cm^2 V^{-1} s^{-1}, respectively, consistent with our earlier results.[27] Both μ_h and μ_e show a fairly broad variation among all devices tested, which is likely due to the inefficient and obstructed injection process from the Au contacts. A large hysteresis in the electron current may result from the presence of electron traps due to air exposure during the device fabrication, but may also arise from poor electron injection properties. Furthermore, the output curves shown in Figure 3(b) are characterized by significant nonohmic behavior in the low-bias regime for both hole and electron currents, indicative of the existence of Schottky-type injection barriers, and are qualitatively in good accordance with the relative energy level alignment shown in Figure 1(c). The electron current does not show saturation behavior at large drain bias. Overall, we find poor and unsatisfactory performance in fm-rubrene SC-OFETs with bottom-contact Au electrodes.

On the other hand, fm-rubrene SC-OFETs with CNT/Au electrodes exhibit substantially enhanced performance. As shown in Figure 3(c), the hole and electron currents I_D in the saturation regime (drain voltage $V_D = -100$ and 100 V) are 1−2 orders of magnitude higher than those in the Au-electrode device (Figure 3(a)), leading to a remarkable μ_h of 4.8 cm^2 V^{-1} s^{-1} and μ_e of 4.2 cm^2 V^{-1} s^{-1}. This electron mobility is already one of the highest values compared with unipolar n-type organic crystals, not to mention an equally large hole mobility.[12,16] To the best of our knowledge, these devices set a new record for ambipolar mobility in wide bandgap, conjugated organic semiconductors.[10,50−53] Additionally, as displayed in Figure 3(d), on the hole transport side, the I_D-V_D behavior in the low bias region becomes nearly ohmic, although not entirely linear, and the same improvement is also prominent in the I_D-V_D curve for electron transport. Furthermore, the

hole/electron current hysteresis becomes almost negligible, indicative of lower concentration of interfacial traps at the fm-rubrene/CNT interface since the fm-rubrene/Cytop interface is unchanged. The output curves for holes and electrons are generally accompanied by negligible noise and current saturation at large V_D, indicating an overall superior performance over devices with Au electrodes. In the case of the CNT electrodes (Section 5, Figure S7 in SI), fm-rubrene transistors performed similarly to the devices with CNT/Au hybrid electrodes, with nearly ohmic behavior for both hole and electron injections, and enhanced ambipolar mobilities (μ_h of 4.2 $cm^2 V^{-1} s^{-1}$ and μ_e of 3.8 $cm^2 V^{-1} s^{-1}$). Another apparent advantage of applying CNT/Au or CNT electrodes was considerably higher ambipolar currents (10^{-7} to 10^{-6} A), making these fm-rubrene devices potentially promising for high-performance light-emitting transistor applications.

The contact resistance (R_C) for hole and electron injection in fm-rubrene SC-OFETs was measured by using the transmission line method (TLM). For the untreated Au electrodes, on the hole-transport side, the total channel resistance ($R \times W$, normalized by width) roughly scales with channel length; however, the electron channel resistance exhibits totally random, anomalous scaling behavior (not shown). In both cases, R_C associated with hole and electron injection are enormous (R_C is ~2741 kΩ-cm for holes at $V_G = -80$ V, $V_D = -40$ V, and R_C is ~498 500 kΩ-cm for electrons at V_G = 120 V, V_D = 80 V). In the case of devices with medium-density CNT/Au electrodes in Figure 4, we find a nearly linear scaling relation between the total channel resistance, $R \times W$, and the channel length L, for both hole and electron transport. R_C for holes and electrons are decreased by several orders of magnitude, where R_C is as low as 7.0 kΩ-cm at $V_G = -80$ V ($V_D = -20$ V) for holes and 109.1 kΩ-cm at V_G = 120 V ($V_D = -60$ V) for electrons. The measured R_C for fm-rubrene OFETs with CNT/Au electrodes are, overall, low for bottom-contact single crystal devices,[1] although more improvement is needed to achieve an entirely linear and ohmic behavior in low bias I_D-V_D characteristics. The R_C values determined from TLM have been confirmed by separate gated four-terminal measurements, which show good agreement between the contact-corrected four-terminal mobility and the saturation mobility (Section 6, Figure S8 in SI). On the basis of the reduced R_C, we conclude that incorporating CNTs as contacts improves the hole and electron injection efficiency simultaneously for wide-bandgap fm-rubrene crystals, leading to enhanced transistor performance and nominally larger, less contact-limited mobility.

In addition, we have fabricated rubrene SC-OFETs using the same device structure as a direct comparison to the fm-rubrene devices (Section 7, Figure S9 in SI). Even with Au electrodes, rubrene devices show ideal transistor behavior, and devices using either CNT/Au or

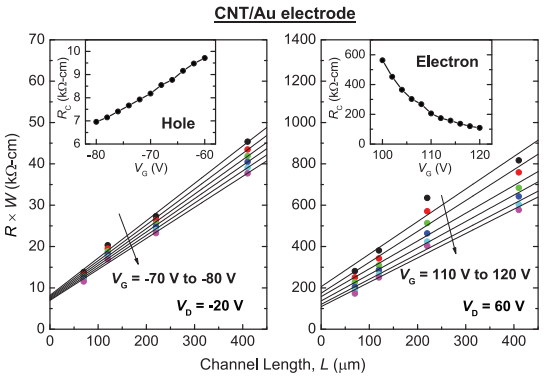

Figure 4. Total channel resistance $R \times W$ (normalized by width) as a function channel length L for hole transport ($V_G = -70$ to -80 V, in 2 V step, at $V_D = -20$ V) and electron transport (V_G = 110 to 120 V, in 2 V step, at V_D = 60 V) in a fm-rubrene SC-OFET with medium-density CNT/Au electrodes. Solid lines (black) are least-squares linear fittings. The contact resistance, R_C, is determined from the intercept (L = 0) of the linear extrapolation. The insets show R_C (normalized by width) as a function of V_G for holes and electrons.

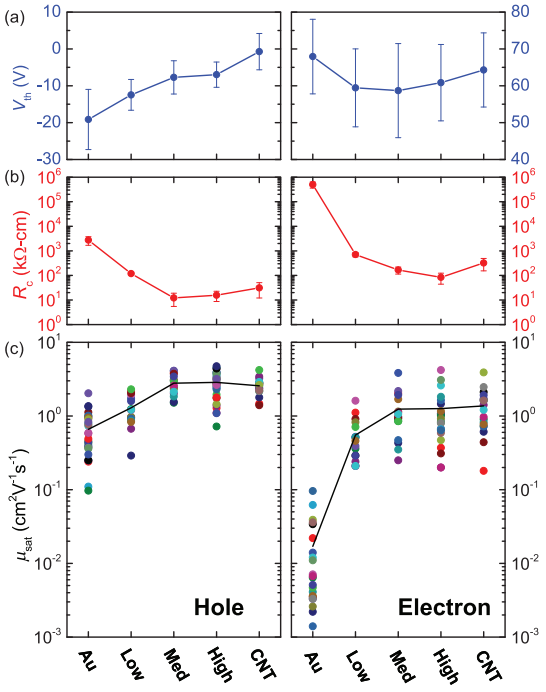

Figure 5. Summary of room-temperature fm-rubrene device properties (Cytop-gated, bottom contact). (a) Hole and electron threshold voltage V_{th}, (b) contact resistance R_C and (c) saturation mobility μ_{sat} as a function of contact conditions. Au: Au electrodes; CNT: CNT electrodes; Low, Med, High: low-density (2−4 CNTs/μm), medium-density (5−15 CNTs/μm) and high-density (>20 CNTs/μm) CNT/Au electrodes. In the mobility panel (c), each round dot represents the individual mobility value for a single device, where solid lines refer to the average mobility values from about 20−40 devices.

CNT electrodes performed equally well, including formation of ohmic contacts as displayed by linear I_D-V_D behavior in the output curves, low contact resistance for holes (R_C ~ 2.1 kΩ-cm at $V_G = -80$ V) and large average μ_h ~ 7.1 $cm^2 V^{-1} s^{-1}$ (best mobility was 10.3 $cm^2 V^{-1} s^{-1}$), consistent with other reports.[41] This

TABLE 1. Summary of Room-Temperature Device Properties for Bottom-Contact, Cytop-Gated fm-Rubrene and Rubrene SC-OFETs[a]

fm-rubrene SC-OFETs

	hole transport				electron transport			
	μ_{sat} ($cm^2 V^{-1} s^{-1}$), average	μ_{sat} ($cm^2 V^{-1} s^{-1}$), max	R_C (kΩ-cm)[b]	V_{th} (V)	μ_{sat} ($cm^2 V^{-1} s^{-1}$), average	μ_{sat} ($cm^2 V^{-1} s^{-1}$), max	R_C (kΩ-cm)[c]	V_{th} (V)
Au	0.66 ± 0.44	2.03	2741 ± 1050	−19.2 ± 8.2	0.017 ± 0.023	0.096	498 500 ± 138 400	67.9 ± 10.1
low CNT/Au	1.29 ± 0.58	2.30	119.5 ± 13.4	−12.5 ± 4.2	0.55 ± 0.38	1.61	709.0 ± 138.6	59.4 ± 10.6
medium CNT/Au	2.78 ± 0.85	4.11	12.2 ± 6.7	−7.7 ± 4.5	1.24 ± 0.89	3.84	167.3 ± 53.5	58.7 ± 12.8
high CNT/Au	2.86 ± 1.11	4.83	15.7 ± 7.0	−7.0 ± 3.4	1.26 ± 0.98	4.20	83.9 ± 39.7	60.9 ± 10.4
CNT	2.57 ± 0.64	4.20	31.4 ± 19.2	−0.7 ± 4.9	1.37 ± 0.84	3.89	322.8 ± 168.4	64.3 ± 10.1

rubrene SC-OFETs

	hole transport				electron transport			
	μ_{sat} ($cm^2 V^{-1} s^{-1}$), average	μ_{sat} ($cm^2 V^{-1} s^{-1}$), max	R_C (kΩ-cm)[d]	V_{th} (V)	μ_{sat} ($cm^2 V^{-1} s^{-1}$), average	μ_{sat} ($cm^2 V^{-1} s^{-1}$), max	R_C (kΩ-cm)	V_{th} (V)
Au	6.65 ± 1.04	8.15	2.1 ± 0.7	6.4 ± 3.4	N/A			
medium CNT/Au	6.79 ± 1.61	9.46	2.5 ± 1.5	10.0 ± 3.5	N/A			
CNT	7.07 ± 1.77	10.3	2.6 ± 0.6	4.2 ± 6.2	N/A			

[a] Au: Au electrodes; CNT: CNT electrodes; low, medium, high: low-density, medium-density, and high-density CNT/Au electrodes. [b] R_C measured at $V_G = -80$ V and $V_D = -20$ V for holes in fm-rubrene SC-OFETs (except for Au electrodes, where R_C is measured at $V_G = -80$ V and $V_D = -40$ V). [c] R_C measured at $V_G = 120$ V and $V_D = 60$ V for electrons in fm-rubrene SC-OFETs (except for Au electrodes, where R_C is measured at $V_G = 120$ V and $V_D = 80$ V). [d] R_C measured at $V_G = -80$ V and $V_D = -20$ V for holes in rubrene SC-OFETs.

is likely because the hole injection and transport properties of rubrene are already outstanding with Au contacts, presumably due to optimal band alignment, therefore the effect of CNT treatment is marginal. Electron transport was barely observed for any case in rubrene transistors (Au, medium-density CNT/Au, CNT electrodes), probably due the presence of a large electron injection barrier (~2.4 eV) that was difficult to surmount. Our strategy of employing CNT electrodes has enabled fm-rubrene transistors to obtain hole mobility up to 4.8 $cm^2 V^{-1} s^{-1}$, which is only a factor of 2 lower than the best hole mobility of rubrene in the present device structure, while the electron mobility (4.2 $cm^2 V^{-1} s^{-1}$) has undoubtedly surpassed rubrene as well as many other small-molecule single crystals.[12,16]

Figure 5 and Table 1 summarize the fm-rubrene SC-OFETs electrical properties (threshold voltage V_{th} in Figure 5(a), contact resistance R_C in Figure 5(b) and saturation hole/electron mobility μ_{sat} in Figure 5(c)) as a function of contact conditions, including Au electrodes, low, medium, and high-density CNT/Au electrodes and CNT electrodes. Overall, an increase in the CNT density leads to a systematic improvement in the device performance up to a CNT density of 5−15/μm. CNT densities exceeding this value do not lead to any additional improvement. Looking at the hole transport, the hole mobility steadily increases as the CNTs are incorporated into the electrodes, and a 4-fold increase in the average mobility is finally achieved when using CNT electrodes. A 100-fold decrease in contact resistance for holes with CNT electrodes supports the hole injection barrier reduction, resulting in the mobility enhancement. Meanwhile, the threshold voltage for hole transport has a favorable shift from −20 V with Au electrodes to almost 0 V using CNT electrodes. The threshold voltage is generally attributed to the amount of deep traps at semiconductor/insulator interface, but since the crystal/Cytop interface does not change, this finding implies the increased injection efficiency can also benefit an earlier and easier device onset. On the other hand, the electron transport has a dramatic improvement with CNT electrodes. In the best case, average electron mobility increases almost 100 times while contact resistance is reduced by 4 orders of magnitude, despite a less significant improvement in the threshold voltage. Additionally, narrower distributions of both hole and electron mobility are clearly seen when using CNT electrodes, indicating consistent and reproducibly efficient charge injection processes. Our study unambiguously points out that substantially more effective injection processes for both holes and electrons have been realized by the use of CNT electrodes, the extent of which increases but eventually saturates with increasing CNT density (*i.e.*, interfacial area of CNT and fm-rubrene). Because of better contacts, the measured hole and electron mobilities have increased significantly, more closely reflecting the intrinsic properties of fm-rubrene crystals.

To elucidate the transport mechanism of fm-rubrene crystals, we have performed variable temperature measurements in devices with engineered contacts. Figure 6 shows the temperature-dependent hole and electron mobility for fm-rubrene SC-OFETs with Au

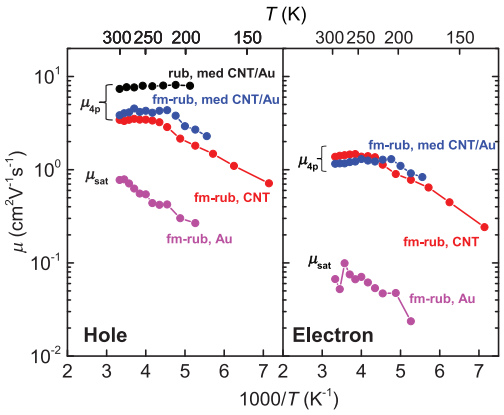

Figure 6. Temperature dependence of hole and electron mobilities for fm-rubrene SC-OFETs with Au electrodes (magenta), CNT electrodes (red), and medium-density CNT/Au electrodes (blue). A rubrene SC-OFET with medium-density CNT/Au electrodes (black) is also shown.

electrodes, medium-density CNT/Au electrodes and CNT electrodes, and a rubrene SC-OFET with medium-density CNT/Au electrodes as a comparison. Four-terminal mobility (μ_{4p}) was adopted to correct for the temperature-dependent R_C, except for the case of fm-rubrene transistor with Au electrodes where R_C was too large to apply the four-terminal structure (μ_{sat} is used). In the rubrene transistor, the hole mobility appears to increase slightly with decreasing temperature, implying a possible band-like transport behavior ($d\mu/dT < 0$), although further evidence (such as Hall effect) is needed. In the fm-rubrene transistor with Au electrodes, hole and electron mobility decrease steadily with decreasing temperature, *i.e.*, they exhibit thermally activated transport with activation energy (E_A) of 50 and 59 meV for holes and electrons, respectively. Comparatively, the hole/electron mobilities of the fm-rubrene transistor with CNT/Au and CNT electrodes stay nearly constant with temperature above 220 K, and in the best case a slight mobility increase is observed, after which mobility starts to decrease with further decreasing temperature. Interestingly, E_A in this regime is also around 50 meV for both holes and electrons, implying that this energy may correspond to the intrinsic shallow trap depth of fm-rubrene crystals, regardless of the injection properties. Temperature-independent transport has been previously observed in other high-mobility organic crystals and thin films.[14,54] Despite the unclear origin of this mobility behavior, the low-temperature ambipolar transport properties in the fm-rubrene device with CNT/Au or CNT electrodes are appreciably improved as compared with Au-contact devices. We anticipate that an intrinsic, band-like transport is likely to be realized in fm-rubrene crystals in the benchmark vacuum-gap structure in which higher mobility is expected (it is known that single crystal mobility is strongly dependent on the dielectric constant of the insulator layer),[17] provided efficient charge injection can also be achieved in the vacuum-gap structure using CNT electrodes.

The utilization of CNTs to improve charge injection has been the subject of research in various organic electronic devices including OLEDs and thin film transistors (OTFTs), in the form of individual CNTs,[28,29] random or aligned CNT networks,[30,31,34,35] or CNT/polymer composites.[32,33] For example, Zaumseil and co-workers have investigated the enhancement of charge injection and light emission in bottom-contact, top-gated polymer ambipolar TFTs, in which CNTs were dispersed within the polymer film at a dilute concentration.[33] Martel and co-workers have reported using embedded hairy CNT contacts for better injection efficiency in bottom-contact n-type and ambipolar PCBM TFTs.[31] In Khondaker's work, lithography-patterned aligned CNT arrays with tunable density have been used as the injection electrodes for high-performance pentacene TFTs.[34,35] Our present experimental studies are the very first application of CNT electrodes to free-standing organic single crystals, in which the contact fabrication techniques are limited due to mechanical fragility and low chemical and environmental tolerance of organic crystals.[55] The extent of improvement in ambipolar charge injection and carrier mobility we have observed in fm-rubrene is unprecedented. Our approach to prepare the CNT-based electrodes by printing is also advantageous because of its simple and lithography-free, room-temperature process. The fact that the CNT-electrode strategy is also successful in organic single crystals suggests that CNTs present a universal mechanism to enhance the injection properties for both types of carriers in a wide variety of organic semiconductor devices.

One explanation for the remarkable and extensive success of the CNT-based electrodes could be related to the conjugated structure of both CNTs and organic crystals, which provides a low trap-density interface beneficial for charge injection.[56] It is well-known that when a metal electrode is in contact with a conjugated organic semiconductor, interfacial states can be induced that not only lead to the formation of interfacial dipoles and a shift of the vacuum level, but also serve as traps that obstruct charge injection.[57] Carbon-based electrodes, such as conducting polymers, graphene, and CNTs, exhibit similar conjugated structure as organic semiconductors, and this may help reduce such an unfavorable interfacial trap state.[58,59] Indeed, the systematic improvement of V_{th} for holes with increasing CNT density (see Figure 5(a)) is supportive of a lower density of hole traps at the CNT-crystal interface compared with Au-crystal interface. A less significant improvement of electron V_{th}, whose optimal value occurs at medium-density CNT coverage (see Figure 5(a)), suggests that, despite the need for more optimization, electron trap density is likewise reduced at the CNT-crystal interface. Nevertheless, we note that other possible mechanisms may also be present that synergistically contribute to the substantial

improvement of ambipolar contact resistance and mobilities.

For example, another explanation could be related to the different work function of CNTs compared with Au. Despite a lack of direct PYS measurements for the CNT film, a work function of ~4.8 eV for single-walled CNTs is assumed on the basis of the literature reports.[60−62] As shown in the energy level diagram in Figure 1(c), for Au electrodes, we can roughly estimate the barrier heights (assuming no interfacial states) for fm-rubrene of Φ_h ~0.9 eV with respect to HOMO level, and of Φ_e ~1.4 eV with respect to LUMO level. Our experimental observations (see Figures 3(a) and (b), and R_C with Au electrodes in Table 1) corroborate easier hole injection than electron injection, but both with large Schottky barriers from Au. While a slightly lower work function of CNTs could possibly explain the improved electron injection in fm-rubrene SC-OFETs using CNT/Au or CNT electrodes, it does not explain the improvement in hole injection, since such a low work function would only increase the hole injection barrier. In the case of CNT electrodes, large Schottky barriers can be presumed, roughly Φ_h ~1.1 eV for holes and Φ_e ~1.2 eV for electrons by assuming Mott−Schottky vacuum-level alignment. Yet, the improvement in ambipolar injection properties suggests that the presence of CNTs at the injection interface leads to nearly electrically transparent barriers for both holes and electrons.

In contrast to transistors with ohmic contacts, in which the channel conduction relies on the gate modulation, for contact-limited transistors, the overall performance is also controlled by the electric field at the contact.[63] As a result, charge injection properties and device performance can be dramatically different by varying the contact geometry. The Au-electrode is better described by using two-dimensional (2D) electrostatics, which has little influence on the local electric field at the contacts (and thus band bending) in the presence of large Schottky barriers. This leads to the absence of tunneling current through the barrier, as manifested by a nonlinear I_D-V_D characteristic and a large R_C. In contrast, because of the form factor of the nanotubes, the CNT-electrode is associated with one-dimensional (1D) electrostatics. In such a scenario, the electric field can be greatly enhanced at the contact region. Simulation results from prior studies have shown the enhancement in the electric field by 1−2 orders of magnitude along the nanotubes and at the tube tips.[33] Therefore, even with large Schottky barriers, nearly ohmic I_D-V_D behavior and reduced contact resistance are achievable because of strong charge carrier tunneling across the barrier, and since the tunneling process is independent of the carrier type, the improvement of injection is effective for both holes and electrons. These conclusions are in line with the observed superior device performance in fm-rubrene SC-OFETs with CNT electrodes as compared to the devices with Au electrodes. Collectively, we speculate that besides CNTs, any low-dimensional conductors such as metal nanowires are also likely to improve the injection properties for holes and electrons in these organic electronic devices whose performance are limited by large Schottky barriers.

CONCLUSIONS

In summary, efficient charge injection, improved transport properties and benchmark hole/electron mobilities have been achieved in ambipolar SC-OFETs based on a new rubrene derivative (fm-rubrene) by employing CNT electrodes. Because of the great enhancement of the electric field along the nanotube in the contact region, holes and electrons can effectively tunnel through the large Schottky barriers formed at the fm-rubrene/electrode interface, leading to a substantial decrease in the contact resistance and nearly ohmic characteristics for both the charge carriers. With engineered contacts, fm-rubrene SC-OFET device performance is approaching its intrinsic, theory-predicted, transport properties. Large and balanced ambipolar mobilities (4.8 $cm^2 V^{-1} s^{-1}$ for holes and 4.2 $cm^2 V^{-1} s^{-1}$ for electrons) and high ambipolar output currents make potential applications of fm-rubrene crystals promising in light-emitting transistors. Indeed, enabling n-type and ambipolar transport with CNT electrodes is an attractive approach for organic semiconductors in general in both fundamental studies and building flexible electronics. Considering the rise in research interest devoted to developing new high-performance organic semiconductors, we point out that fabricating good contacts and optimizing the charge injection are as critical to achieving the ultimate electrical performance of the semiconductor material as rational molecular design and proper semiconductor processing methods.

METHODS

Single Crystal Growth. Rubrene powders (sublimed grade) were purchased from Sigma-Aldrich (Milwaukee, WI). Fm-rubrene source materials were synthesized and purified on the basis of previously established methods.[27] Single crystals were grown from vapor phase using horizontal physical vapor transport.[36] Ultrapure Ar was used as the carrier gas. Very thin crystals (thickness <1 μm) were obtained after short time growth at slightly higher temperatures (for rubrene, 1-h growth at 300 °C; for fm-rubrene, 3-h growth at 270 °C). Individual crystals with clean surfaces were selected for the subsequent device fabrications.

Ultraviolet Photoelectron Spectroscopy. UPS measurements were conducted at Beamline BL-13A in the Photon Factory, KEK.[64] The excitation photon energy was set at 30 eV and photoelectrons were collected by a two-dimensional electron

spectrometer (Scienta SES200). To avoid photoemission-induced sample charging during the measurements, each crystal sample was bonded onto an Au-coated Si wafer by encircling with Ag paste and was illuminated by continuous-wave laser light (405 nm, 30 mW for rubrene; 375 nm, 10 mW for fm-rubrene) to enhance photoconductivity.[37]

Photoelectron Yield Spectroscopy. PYS measurements were carried out in a home-built system.[65] Ultraviolet white light from a 150 W deuterium discharge lamp was monochromatized by a doubled grating and focused onto the sample in N_2 atmosphere. The details of the photoemission detection system will be found elsewhere.[38] Crystals of typically 10 mm × 10 mm size fixed by carbon tape onto Si wafers were adopted as specimens, while the excitation light was focused within the crystal area (*ca.* 2 mm × 5 mm).

Carbon Nanotube Preparation. Single walled carbon nanotubes (CNTs), synthesized by arc discharge (P2, Carbon Solutions) with an average diameter of 1.4 nm, were horn sonicated in a solution of 1−2 wt % sodium cholate (SC) in deionized water (DI). The solution was then centrifuged at 15 000 rpm for 45 min to remove any material that was not well dispersed. The supernatant was decanted and the resulting solution was diluted with an aqueous solution of 1−2 wt % SC resulting in concentrations ranging from 0.1−5 mg/mL, as determined from optical absorbance spectroscopy.

Fabrication of SC-OFETs. Highly p-doped SiO_2(300 nm)/Si wafers (resistivity 0.005 − 0.01 Ω-cm, thickness 525 μm) purchased from Silicon Valley Microelectronics, Inc. (US) were used as the substrates and also served as the gate electrodes. On top of that, we spin-coated a thin layer of Cytop (CTL809M, Asashi Glass Co., Ltd.) using diluted volume ratio 1:10 solution of CTL-809M: CT-solvent at 2000 rpm for 60 s and postbaked at 120 °C for 1 h. The resulting Cytop films were about 30−40 nm in thickness, as determined by a VASE ellipsometer (J.A. Wollam Co., Inc.). The total dielectric capacitance was about 9×10^{-9} F/cm^2 contributed by both the SiO_2 ($\varepsilon_r = 3.9$) and Cytop ($\varepsilon_r = 2.2$), and this capacitance value was confirmed in an Au-insulator-Au structure in a separate impedance measurement using HP 4192A impedance analyzer (at zero DC bias, AC oscillation of 100 mV and AC frequency of 1 kHz). Gold source and drain contacts (40 nm) were then thermally evaporated on top of the Cytop layer through stainless-steel shadow masks in a home-built thermal evaporator (base pressure 7×10^{-7} Torr). Typical channel length was 500 μm (in TLM, channel lengths were 420, 220, 110, and 70 μm). The printing process for water-based CNT inks was accomplished in ambient conditions using a commercially available table-top aerosol jet printing system (Optomec, Inc.). Substrates were heated at 60 °C during printing to dry the solvent. Printing speed was typically 2 mm/s. Printed CNTs covered the entire Au electrode area and also were intentionally printed at the edge of Au/Cytop such that they slightly extended into the channel. After that, the substrates were gently rinsed with deionized (DI) water to remove residual sodium cholate (SC) and were then allowed to dry at 100 °C for 2 h in a vacuum oven. This process, usually repeated twice, resulted in a randomly oriented CNT network with various densities sparsely distributed on Au (Figure 2), denoted as the CNT/Au electrodes. In a separate protocol, a concentrated CNT ink was printed on top of Au, resulting in a visible, thick, and dense bundled film, which could not be washed away by deionized water, and was used as the CNT electrodes. To complete the SC-OFETs, thin crystals were finally laminated across the source and drain electrodes, where contacts were formed by spontaneous adhesion of crystals onto the substrates, or with the help of applying gate bias. Devices were fabricated on a benchtop and were then immediately transferred into a N_2-filled glovebox for electrical measurements.

Electrical Measurements. Device characteristics of SC-OFETs were measured in a Desert Cryogenics (Lakeshore, Inc.) vacuum probe station in a N_2-filled glovebox with Keithley 236/237 and 6517A electrometers and homemade LabVIEW programs. Low temperature measurements employed a Lakeshore 331 temperature controller so that the ramp rate was under control. Cooling rate was kept at about 0.5 K/min to minimize the differential strain between crystals and substrates during the cooling process. All measurements were carried out in the dark and in a vacuum at a pressure $\sim 10^{-6}$ Torr.

The field-effect mobilities were calculated in the saturation regime ($V_D = -100$ V for holes and $V_D = 100$ V for electrons), *i.e.*, in the unipolar regimes for holes and electrons, respectively, on the basis of the following equation: $I_D(\text{sat}) = (W/2L)\mu C_i(V_G - V_{th})^2$ and $(\partial(I_D)^{1/2}/\partial V_G) = ((W/2L)\mu C_i)^{1/2}$, where I_D is the drain current (A), V_D is the drain voltage (V), V_G is the gate voltage (V), V_{th} is the threshold voltage (V), μ is the field-effect mobility (cm^2 V^{-1} s^{-1}), C_i is the specific capacitance of insulator layer (F/cm^2), and W and L are the channel width and length (μm).

SEM Imaging. SEM images of the CNT morphology were acquired using a JEOL 6500 Field-emission gun scanning electron microscope system at typically 5 kV accelerating voltage and 10 mm working distance.

Conflict of Interest: The authors declare no competing financial interest.

Acknowledgment. This work was supported by the MRSEC program of the National Science Foundation at University of Minnesota under Award Number DMR-0819885. W.X. would like to thank the University of Minnesota for financial support through a Doctoral Dissertation Fellowship during this work. Parts of this work were carried out in the Characterization Facility, University of Minnesota, which receives partial support from NSF through the MRSEC program. M.C.H. would like to thank the Office of Naval Research MURI Program (N00014-11-1-0690) for supporting P.L.P. and M.L.G. A National Science Foundation Graduate Research Fellowship (M.L.G.) is also acknowledged. UPS studies were done under the approval of the PF Program Advisory Committee (2011G161 and 2013G135). Y.N. would like to thank support from KAKENHI (23750209) from the Japan Society for the Promotion of Science (JSPS) and G-COE program of Chiba University (Advanced School for Organic Electronics; G-3). H.I. would like to thank support by JSPS through the "Funding Program for World-Leading Innovative R&D on Science and Technology (FIRST Program)" initiated by the Council for Science and Technology Policy. C.J.D. would like to thank DuPont for a Young Faculty Award. K.A.M. would like to thank Victor G. Young, Jr. for helpful guidance on single-crystal XRD.

Supporting Information Available: Single crystal X-ray diffraction of vapor-grown fm-rubrene crystals. Surface dipoles in rubrene and fm-rubrene crystals. Characterization of CNT solutions. SEM images of CNT/Au electrodes and CNT electrodes. Device performance of fm-rubrene SC-OFETs with CNT electrodes. Four-terminal measurement in fm-rubrene SC-OFETs. Device performance of rubrene SC-OFETs with different electrodes. This material is available free of charge *via* the Internet at http://pubs.acs.org.

REFERENCES AND NOTES

1. Bao, Z.; Locklin, J. *Organic Field-Effect Transistor*; CRC Press: Boca Raton, FL, 2007.
2. Ishii, H.; Sugiyama, K.; Ito, E.; Seki, K. Energy Level Alignment and Interfacial Electronic Structures at Organic/Metal and Organic/Organic Interfaces. *Adv. Mater.* **1999**, *11*, 605–625.
3. Gershenson, M. E.; Podzorov, V.; Morpurgo, A. F. Colloquium: Electronic Transport in Single-Crystal Organic Transistors. *Rev. Mod. Phys.* **2006**, *78*, 973–989.
4. de Boer, B.; Hadipour, A.; Mandoc, M. M.; van Woudenbergh, T.; Blom, P. W. M. Tuning of Metal Work Functions with Self-Assembled Monolayers. *Adv. Mater.* **2005**, *17*, 621–625.
5. Hamadani, B. H.; Corley, D. A.; Ciszek, J. W.; Tour, J. M.; Natelson, D. Controlling Charge Injection in Organic Field-Effect Transistors Using Self-Assembled Monolayers. *Nano Lett.* **2006**, *6*, 1303–1306.
6. Zhou, Y.; Fuentes-Hernandez, C.; Shim, J.; Meyer, J.; Giordano, A. J.; Li, H.; Winget, P.; Papadopoulos, T.; Cheun, H.; Kim, J.; *et al.* A Universal Method to Produce Low-Work Function Electrodes for Organic Electronics. *Science* **2012**, *336*, 327–332.

7. Soeda, J.; Hirose, Y.; Yamagishi, M.; Nakao, A.; Uemura, T.; Nakayama, K.; Uno, M.; Nakazawa, Y.; Takimiya, K.; Takeya, J. Solution-Crystallized Organic Field-Effect Transistors with Charge-Acceptor Layers: High-Mobility and Low-Threshold-Voltage Operation in Air. *Adv. Mater.* **2011**, *23*, 3309–3314.
8. Kitamura, Y.; Shikoh, E.; Sawabe, K.; Takenobu, T.; Shiraishi, M. Realization of Ohmic-Like Contact between Ferromagnet and Rubrene Single Crystal. *Appl. Phys. Lett.* **2012**, *101*, 073501.
9. Minari, T.; Darmawan, P.; Liu, C.; Li, Y.; Xu, Y.; Tsukagoshi, K. Highly Enhanced Charge Injection in Thienoacene-Based Organic Field-Effect Transistors with Chemically Doped Contact. *Appl. Phys. Lett.* **2012**, *100*, 093303.
10. Gwinner, M. C.; Vaynzof, Y.; Banger, K. K.; Ho, P. K. H.; Friend, R. H.; Sirringhaus, H. Solution-Processed Zinc Oxide as High-Performance Air-Stable Electron Injector in Organic Ambipolar Light-Emitting Field-Effect Transistors. *Adv. Funct. Mater.* **2010**, *20*, 3457–3465.
11. Darmawan, P.; Minari, T.; Kumatani, A.; Li, Y.; Liu, C.; Tsukagoshi, K. Reduction of Charge Injection Barrier by 1-nm Contact Oxide Interlayer in Organic Field Effect Transistors. *Appl. Phys. Lett.* **2012**, *100*, 013303.
12. Menard, E.; Podzorov, V.; Hur, S. H.; Gaur, A.; Gershenson, M. E.; Rogers, J. A. High-Performance n- and p-Type Single-Crystal Organic Transistors with Free-Space Gate Dielectrics. *Adv. Mater.* **2004**, *16*, 2097–2101.
13. Xie, H.; Alves, H.; Morpurgo, A. F. Quantitative Analysis of Density-Dependent Transport in Tetramethyltetraselenafulvalene Single-Crystal Transistors: Intrinsic Properties and Trapping. *Phys. Rev. B: Condens. Matter Mater. Phys.* **2009**, *80*, 245305.
14. Xie, W.; Willa, K.; Wu, Y.; Häusermann, R.; Takimiya, K.; Batlogg, B.; Frisbie, C. D. Temperature-Independent Transport in High-Mobility Dinaphtho-Thieno-Thiophene (DNTT) Single Crystal Transistors. *Adv. Mater.* **2013**, *25*, 3478–3484.
15. Xie, W.; McGarry, K. A.; Liu, F.; Wu, Y.; Ruden, P. P.; Douglas, C. J.; Frisbie, C. D. High-Mobility Transistors Based on Single Crystals of Isotopically Substituted Rubrene-d_{28}. *J. Phys. Chem. C* **2013**, *117*, 11522–11529.
16. Minder, N. A.; Ono, S.; Chen, Z.; Facchetti, A.; Morpurgo, A. F. Band-Like Electron Transport in Organic Transistors and Implication of the Molecular Structure for Performance Optimization. *Adv. Mater.* **2012**, *24*, 503–508.
17. Hulea, I. N.; Fratini, S.; Xie, H.; Mulder, C. L.; Iossad, N. N.; Rastelli, G.; Ciuchi, S.; Morpurgo, A. F. Tunable Fröhlich Polarons in Organic Single-Crystal Transistors. *Nat. Mater.* **2006**, *5*, 982–986.
18. Podzorov, V.; Sysoev, S. E.; Loginova, E.; Pudalov, V. M.; Gershenson, M. E. Single-Crystal Organic Field Effect Transistors with the Hole Mobility ~8 cm^2/Vs. *Appl. Phys. Lett.* **2003**, *83*, 3504.
19. Calhoun, M. F.; Sanchez, J.; Olaya, D.; Gershenson, M. E.; Podzorov, V. Electronic Functionalization of the Surface of Organic Semiconductors with Self-Assembled Monolayers. *Nat. Mater.* **2007**, *7*, 84–89.
20. Podzorov, V.; Menard, E.; Borissov, A.; Kiryukhin, V.; Rogers, J. A.; Gershenson, M. E. Intrinsic Charge Transport on the Surface of Organic Semiconductors. *Phys. Rev. Lett.* **2004**, *93*, 086602.
21. Podzorov, V.; Menard, E.; Rogers, J. A.; Gershenson, M. E. Hall Effect in the Accumulation Layers on the Surface of Organic Semiconductors. *Phys. Rev. Lett.* **2005**, *95*, 226601.
22. Xia, Y.; Xie, W.; Ruden, P. P.; Frisbie, C. D. Carrier Localization on Surfaces of Organic Semiconductors Gated with Electrolytes. *Phys. Rev. Lett.* **2010**, *105*, 036802.
23. Xie, W.; Frisbie, C. D. Organic Electrical Double Layer Transistors Based on Rubrene Single Crystals: Examining Transport at High Surface Charge Densities above 10^{13} cm^{-2}. *J. Phys. Chem. C* **2011**, *115*, 14360–14368.
24. Xie, W.; Frisbie, C. D. Electrolyte Gated Single-Crystal Organic Transistors to Examine Transport in the High Carrier Density Regime. *MRS Bull.* **2013**, *38*, 43–50.
25. Najafov, H.; Lee, B.; Zhou, Q.; Feldman, L. C.; Podzorov, V. Observation of Long-Range Exciton Diffusion in Highly Ordered Organic Semiconductors. *Nat. Mater.* **2010**, *9*, 938–943.
26. Najafov, H.; Mastrogiovanni, D.; Garfunkel, E.; Feldman, L. C.; Podzorov, V. Photon-Assisted Oxygen Diffusion and Oxygen-Related Traps in Organic Semiconductors. *Adv. Mater.* **2011**, *23*, 981–985.
27. McGarry, K. A.; Xie, W.; Sutton, C.; Risko, C.; Wu, Y.; Young, V. G.; Brédas, J.-L.; Frisbie, C. D.; Douglas, C. J. Rubrene-Based Single-Crystal Organic Semiconductors: Synthesis, Electronic Structure, and Charge-Transport Properties. *Chem. Mater.* **2013**, *25*, 2254–2263.
28. Qi, P.; Javey, A.; Rolandi, M.; Wang, Q.; Yenilmez, E.; Dai, H. Miniature Organic Transistors with Carbon Nanotubes as Quasi-One-Dimensional Electrodes. *J. Am. Chem. Soc.* **2004**, *126*, 11774–11775.
29. Aguirre, C. M.; Ternon, C.; Paillet, M.; Desjardins, P.; Martel, R. Carbon Nanotubes as Injection Electrodes for Organic Thin Film Transistors. *Nano Lett.* **2009**, *9*, 1457–1461.
30. Liu, B.; McCarthy, M. A.; Yoon, Y.; Kim, D. Y.; Wu, Z.; So, F.; Holloway, P. H.; Reynolds, J. R.; Guo, J.; Rinzler, A. G. Carbon-Nanotube-Enabled Vertical Field Effect and Light-Emitting Transistors. *Adv. Mater.* **2008**, *20*, 3605–3609.
31. Cicoira, F.; Aguirre, C. M.; Martel, R. Making Contacts to n-Type Organic Transistors Using Carbon Nanotube Arrays. *ACS Nano* **2011**, *5*, 283–290.
32. Hellstrom, S. L.; Jin, R. Z.; Stoltenberg, R. M.; Bao, Z. Driving High-Performance n- and p-Type Organic Transistors with Carbon Nanotube/Conjugated Polymer Composite Electrodes Patterned Directly from Solution. *Adv. Mater.* **2010**, *22*, 4204–4208.
33. Gwinner, M. C.; Jakubka, F.; Gannott, F.; Sirringhaus, H.; Zaumseil, J. Enhanced Ambipolar Charge Injection with Semiconducting Polymer/Carbon Nanotube Thin Films for Light-Emitting Transistors. *ACS Nano* **2012**, *6*, 539–548.
34. Sarker, B. K.; Khondaker, S. I. Thermionic Emission and Tunneling at Carbon Nanotube−Organic Semiconductor Interface. *ACS Nano* **2012**, *6*, 4993–4999.
35. Kang, N.; Sarker, B. K.; Khondaker, S. I. The Effect of Carbon Nanotube/Organic Semiconductor Interfacial Area on the Performance of Organic Transistors. *Appl. Phys. Lett.* **2012**, *101*, 233302.
36. Laudise, R. A.; Kloc, C.; Simpkins, P. G.; Siegrist, T. Physical Vapor Growth of Organic Semiconductors. *J. Cryst. Growth* **1998**, *187*, 449–454.
37. Machida, S.; Nakayama, Y.; Duhm, S.; Xin, Q.; Funakoshi, A.; Ogawa, N.; Kera, S.; Ueno, N.; Ishii, H. Highest-Occupied-Molecular-Orbital Band Dispersion of Rubrene Single Crystals as Observed by Angle-Resolved Ultraviolet Photoelectron Spectroscopy. *Phys. Rev. Lett.* **2010**, *104*, 156401.
38. Nakayama, Y.; Machida, S.; Minari, T.; Tsukagishi, K.; Noguchi, Y.; Ishii, H. Direct Observation of the Electronic States of Single Crystalline Rubrene under Ambient Condition by Photoelectron Yield Spectroscopy. *Appl. Phys. Lett.* **2008**, *93*, 173305.
39. Nakayama, Y.; Machida, S.; Tsunami, D.; Kimura, Y.; Niwano, M.; Noguchi, Y.; Ishii, H. Photoemission Measurement of Extremely Insulating Materials: Capacitive Photocurrent Detection in Photoelectron Yield Spectroscopy. *Appl. Phys. Lett.* **2008**, *92*, 153306.
40. Takimiya, K.; Shinamura, S.; Osaka, I.; Miyazaki, E. Thienoacene-Based Organic Semiconductors. *Adv. Mater.* **2011**, *23*, 4347–4370.
41. Kalb, W. L.; Mathis, T.; Haas, S.; Stassen, A. F.; Batlogg, B. Organic Small Molecule Field-Effect Transistors with Cytop Gate Dielectric: Eliminating Gate Bias Stress Effects. *Appl. Phys. Lett.* **2007**, *90*, 092104.
42. Cho, J. H.; Lee, J.; Xia, Y.; Kim, B.; He, Y.; Renn, M. J.; Lodge, T. P.; Frisbie, C. D. Printable Ion-Gel Gate Dielectrics for Low-Voltage Polymer Thin-Film Transistors on Plastic. *Nat. Mater.* **2008**, *7*, 900–906.
43. Xia, Y.; Zhang, W.; Ha, M.; Cho, J. H.; Renn, M. J.; Kim, C. H.; Frisbie, C. D. Printed Sub-2 V Gel-Electrolyte-Gated Polymer Transistors and Circuits. *Adv. Funct. Mater.* **2010**, *20*, 587–594.
44. Ha, M.; Xia, Y.; Green, A. A.; Zhang, W.; Renn, M. J.; Kim, C. H.; Hersam, M. C.; Frisbie, C. D. Printed, Sub-3V Digital

Circuits on Plastic from Aqueous Carbon Nanotube Inks. *ACS Nano* **2010**, *4*, 4388–4395.
45. Ha, M.; Seo, J.-W. T.; Prabhumirashi, P. L.; Zhang, W.; Geier, M. L.; Renn, M. J.; Kim, C. H.; Hersam, M. C.; Frisbie, C. D. Aerosol Jet Printed, Low Voltage, Electrolyte Gated Carbon Nanotube Ring Oscillators with Sub-5 μs Stage Delays. *Nano Lett.* **2013**, *13*, 954–960.
46. Wang, C.; Chien, J.-C.; Takei, K.; Takahashi, T.; Nah, J.; Niknejad, A. M.; Javey, A. Extremely Bendable, High-Performance Integrated Circuits Using Semiconducting Carbon Nanotube Networks for Digital, Analog, and Radio-Frequency Applications. *Nano Lett.* **2012**, *12*, 1527–1533.
47. Engel, M.; Small, J. P.; Steiner, M.; Freitag, M.; Green, A. A.; Hersam, M. C.; Avouris, P. Thin Film Nanotube Transistors Based on Self-Assembled, Aligned, Semiconducting Carbon Nanotube Arrays. *ACS Nano* **2008**, *2*, 2445–2452.
48. Wang, C.; Zhang, J.; Ryu, K.; Badmaev, A.; de Arco, L. G.; Zhou, C. Wafer-Scale Fabrication of Separated Carbon Nanotube Thin-Film Transistors for Display Applications. *Nano Lett.* **2009**, *9*, 4285–4291.
49. Geier, M. L.; Prabhumirashi, P. L.; McMorrow, J. J.; Xu, W.; Seo, J.-W. T.; Everaerts, K.; Kim, C. H.; Marks, T. J.; Hersam, M. C. Subnanowatt Carbon Nanotube Complementary Logic Enabled by Threshold Voltage Control. *Nano Lett.* **2013**, *13*, 4810–4814.
50. Takenobu, T.; Bisri, S.; Takahashi, T.; Yahiro, M.; Adachi, C.; Iwasa, Y. High Current Density in Light-Emitting Transistors of Organic Single Crystals. *Phys. Rev. Lett.* **2008**, *100*, 066601.
51. Bisri, S. Z.; Takenobu, T.; Yomogida, Y.; Shimotani, H.; Yamao, T.; Hotta, S.; Iwasa, Y. High Mobility and Luminescent Efficiency in Organic Single-Crystal Light-Emitting Transistors. *Adv. Funct. Mater.* **2009**, *19*, 1728–1735.
52. Yomogida, Y.; Pu, J.; Shimotani, H.; Ono, S.; Hotta, S.; Iwasa, Y.; Takenobu, T. Ambipolar Organic Single-Crystal Transistors Based on Ion Gels. *Adv. Mater.* **2012**, *24*, 4392–4397.
53. Zaumseil, J.; Sirringhaus, H. Electron and Ambipolar Transport in Organic Field-Effect Transistors. *Chem. Rev.* **2007**, *107*, 1296–1323.
54. Li, J.; Zhao, Y.; Tan, H. S.; Guo, Y.; Di, C.-A.; Yu, G.; Liu, Y.; Lin, M.; Lim, S. H.; Zhou, Y.; *et al.* A Stable Solution-Processed Polymer Semiconductor with Record High-Mobility for Printed Transistors. *Sci. Rep.* **2012**, *2*, 754.
55. de Boer, R. W. I.; Gershenson, M. E.; Morpurgo, A. F.; Podzorov, V. Organic Single-Crystal Field-Effect Transistors. *Phys. Status Solidi A* **2004**, *201*, 1302–1331.
56. Valitova, I.; Amato, M.; Mahvash, F.; Cantele, G.; Maffucci, A.; Santato, C.; Martel, R.; Cicoira, F. Carbon Nanotube Electrodes in Organic Transistors. *Nanoscale* **2013**, *5*, 4638.
57. Kahn, A.; Koch, N.; Gao, W. Electronic Structure and Electrical Properties of Interfaces Between Metals and π-Conjugated Molecular Films. *J. Polym. Sci., Part B: Polym. Phys.* **2003**, *41*, 2529–2548.
58. Koch, N.; Vollmer, A. Electrode-Molecular Semiconductor Contacts: Work-Function-Dependent Hole Injection Barriers *versus* Fermi-Level Pinning. *Appl. Phys. Lett.* **2006**, *89*, 162107.
59. Lee, S.; Jo, G.; Kang, S.-J.; Wang, G.; Choe, M.; Park, W.; Kim, D.-Y.; Kahng, Y. H.; Lee, T. Enhanced Charge Injection in Pentacene Field-Effect Transistors with Graphene Electrodes. *Adv. Mater.* **2011**, *23*, 100–105.
60. Tanaka, Y.; Hirana, Y.; Niidome, Y.; Kato, K.; Saito, S.; Nakashima, N. Experimentally Determined Redox Potentials of Individual (n,m) Single-Walled Carbon Nanotubes. *Angew. Chem., Int. Ed.* **2009**, *48*, 7655–7659.
61. Liu, P.; Sun, Q.; Zhu, F.; Liu, K.; Jiang, K.; Liu, L.; Li, Q.; Fan, S. Measuring the Work Function of Carbon Nanotubes with Thermionic Method. *Nano Lett.* **2008**, *8*, 647–651.
62. Suzuki, S.; Watanabe, Y.; Homma, Y.; Fukuba, S.; Heun, S.; Locatelli, A. Work Functions of Individual Single-Walled Carbon Nanotubes. *Appl. Phys. Lett.* **2004**, *85*, 127–129.
63. Heinze, S.; Tersoff, J.; Martel, R.; Derycke, V.; Appenzeller, J.; Avouris, P. Carbon Nanotubes as Schottky Barrier Transistors. *Phys. Rev. Lett.* **2002**, *89*, 106801.
64. Toyoshima, A.; Kikuchi, T.; Tanaka, H.; Mase, K.; Amemiya, K.; Ozawa, K. Performance of PF BL-13A, a Vacuum Ultraviolet and Soft X-Ray Undulator Beamline for Studying Organic Thin Films Adsorbed on Surfaces. *J. Phys.: Conf. Ser.* **2013**, *425*, 152019.
65. Machida, S.; Ozawa, Y.; Takahashi, J.; Tokairin, H.; Nakayama, Y.; Ishii, H. Low-Energy Photoemission Study of C_{60}/Rubrene/Au Interfaces in Practical Device Thickness. *Appl. Phys. Express* **2013**, *6*, 025801.